



Contents lists available at ScienceDirect

## Quaternary Science Reviews

journal homepage: [www.elsevier.com/locate/quascirev](http://www.elsevier.com/locate/quascirev)

# Paleoclimate change in Ethiopia around the last interglacial derived from annually-resolved stalagmite evidence

Asfawossen Asrat<sup>a,\*</sup>, Andy Baker<sup>b,c</sup>, Melanie J. Leng<sup>d,e</sup>, John Hellstrom<sup>f</sup>,  
Gregoire Mariethoz<sup>g</sup>, Ian Boomer<sup>h</sup>, Dorothy Yu<sup>i</sup>, Catherine N. Jex<sup>j</sup>, John Gunn<sup>h</sup>

<sup>a</sup> School of Earth Sciences, Addis Ababa University, P. O. Box. 1176, Addis Ababa, Ethiopia

<sup>b</sup> PANGAEA Research Centre, School of Biological, Earth and Environmental Sciences, UNSW Sydney, Sydney, NSW, 2052, Australia

<sup>c</sup> ARC Centre of Excellence for Australian Biodiversity and Heritage, Australia

<sup>d</sup> NERC Isotope Geosciences Facility, British Geological Survey, Keyworth, UK

<sup>e</sup> School of Biosciences, University of Nottingham, UK

<sup>f</sup> School of Earth Sciences, University of Melbourne, Parkville, VIC, 3052, Australia

<sup>g</sup> Institute of Earth Surface Dynamics, University of Lausanne, CH-1015, Switzerland

<sup>h</sup> School of Geography, Earth and Environmental Sciences, University of Birmingham, Edgbaston, Birmingham, UK

<sup>i</sup> Mark Wainwright Analytical Centre, UNSW Sydney, Sydney, 2052, Australia

<sup>j</sup> ScienceNordic, Carl Jacobsens Vej 16, 2500, Valby, Copenhagen, Denmark

## ARTICLE INFO

## Article history:

Received 20 January 2018

Received in revised form

18 May 2018

Accepted 13 June 2018

Available online xxx

## Keywords:

Last interglacial

Northeast Africa

Speleothem

Oxygen isotopes

Paleoclimate

## ABSTRACT

Oxygen and carbon ( $\delta^{18}\text{O}/\delta^{13}\text{C}$ ) isotope, growth rate and trace element data are reported for a U-Th dated, annually-laminated stalagmite, GM1 from Goda Mea Cave, Ethiopia. The stalagmite grew intermittently around the last interglacial. The proxy records are used to develop a conceptual growth model of the stalagmite and to assess its potential for revealing a climate signal in this climatically sensitive north-eastern African region during an important period in the evolution of *Homo sapiens* and dispersal of Anatomically Modern Humans out of Africa. Speleothem deposition is of short-duration occurring at ~129 ka, ~120 ka, in an undated growth phase, and at ~108 ka; probably due to tectonic activity.  $\delta^{18}\text{O}$  composition is very stable within growth phases ( $1\sigma$  variability < 0.76‰), as are Mg/Ca, Sr/Ca and Ba/Ca, all indicative of well-mixed source-waters. A shift to positive  $\delta^{18}\text{O}$  values and increased variability in Mg/Ca, Sr/Ca and Ba/Ca prior to growth hiatuses is observed, indicating a loss of the well-mixed water source prior to growth cessation. Mean  $\delta^{18}\text{O}$  composition (−3.82 to −7.77‰) is lower than published modern and Holocene stalagmites from the region. Geochemical data, statistical analyses, and a conceptual model of stalagmite growth, demonstrate that climatic conditions recorded by GM1 were wetter than the Holocene. The ~129 ka growth phase particularly presents an annual record of the relative Intertropical Convergence Zone (ITCZ) position. The GM1 record, the oldest high-resolution continental climate record from Ethiopia so far published, presents evidence that any early human migrations which occurred during MIS 5 are likely to have occurred during a wet event in northeast Africa.

© 2018 Elsevier Ltd. All rights reserved.

## 1. Introduction

In Ethiopia, stalagmites provide high-resolution records of past climate and environment (Asrat et al., 2007; Baker et al., 2007, 2010). Fast-growing, annually-laminated stalagmites are ubiquitous, due to the strong seasonality of rainfall and the water balance in Ethiopia. Regular laminae, visible in hand section, can provide

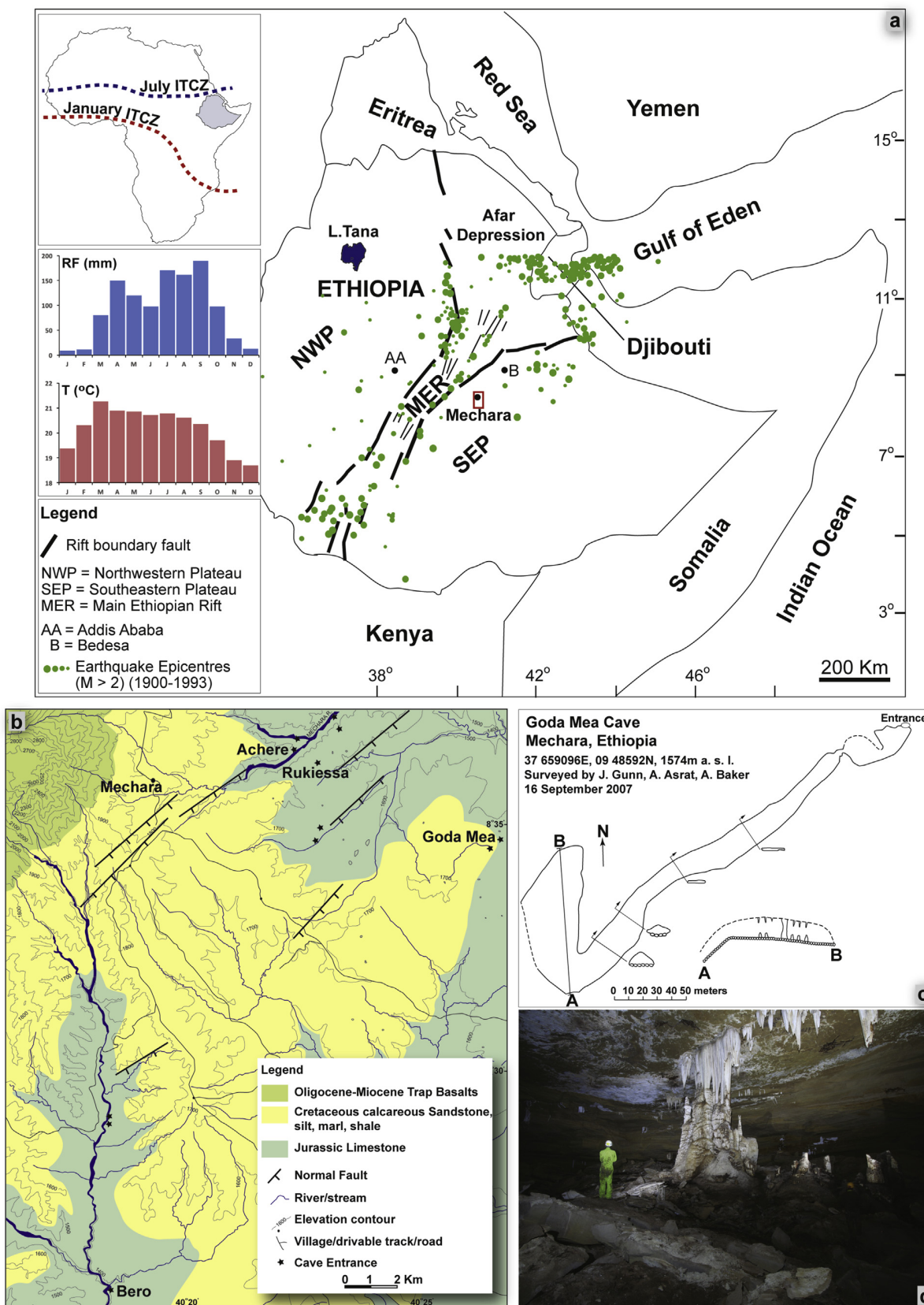
precise annual chronology. Annual growth rates of these stalagmites, determined from the thickness of an annual lamina, is at the upper range of those observed in stalagmites (typically ~0.5 mm/yr). This is due to the optimal climatic conditions (high temperature and rainfall) for limestone dissolution and re-precipitation. This rapid growth facilitates the high-resolution sampling of stalagmite calcite.

\* Corresponding author.

E-mail address: [asfawossen.asrat@aaau.edu.et](mailto:asfawossen.asrat@aaau.edu.et) (A. Asrat).

<https://doi.org/10.1016/j.quascirev.2018.06.016>

0277-3791/© 2018 Elsevier Ltd. All rights reserved.



In Ethiopia, the real advantage of using speleothems to provide a paleoclimate proxy record is that they contain information on past rainfall variability in the region. Several major air streams and convergence zones influence the current climate pattern in northeast Africa, whose effects are often compounded by such regional factors as topography and the proximity to the oceans (e.g., Nicholson, 1996). The relatively dry north-easterly and south-easterly monsoons and the humid and moisture-laden (rainfall generating), westerly and south-westerly air flow of the Congo air stream, generally dominate the regional wind and pressure patterns. The Intertropical Convergence Zone (ITCZ) and the Congo Air Boundary (CAB) separate these major air streams. The passage of the ITCZ (Fig. 1a) dominantly determines the rainy seasons in Ethiopia, while the topography (highland barriers separated by a rift zone) modulates the local rainfall distribution. Accordingly, Ethiopian climate has two rainy seasons, one from the northward passage of the ITCZ, called locally the ‘big rains’ (between June and September), which is reliable and whose maxima migrates with the position of the ITCZ. A second rainy season, the ‘small rains’, is less consistent and occurs between March and May with maxima in April. Dryland farming, including subsistence farming, leads to a high dependency on rains in both seasons. Failure of the ‘small’ rains is common and has occurred in recent years in 2013/2014 and 2015/2016, particularly in the southeastern Ethiopian lowlands bordering the current study area. The climate dynamical cause of the failure of the ‘small’ rains, and how this varies over time, is still poorly understood.

In addition, reliable, high-resolution climate records beyond the Holocene are scarce in the northeastern African region, one of the major candidates for the origin of *Homo sapiens* and a gateway to the “out of Africa” migration of our species during the late Pleistocene. The influence of climate on the dispersal of Anatomically Modern Humans from northeastern Africa particularly during the period ~120 to ~50 ka has been a subject of intense discussion (e.g., Tierney et al., 2017 and references therein; Lamb et al., 2018). Recent discovery of *Homo sapiens* fossils dated to 177 to 194 ka in the Misliya cave in Israel (Hershkovitz et al., 2018) indicates that the “out of Africa” migration episodes have started earlier than the previously thought period of migration (~120–50 ka). Discussions on influence of climate on human dispersal often rely on marine climate records from the Indian Ocean and Mediterranean Sea. The recently published Lake Tana record from the northwestern Ethiopian highland, largely covering the last ~150 ka (Lamb et al., 2018) is the only continental record available. In this paper, we present a high-resolution continental climate record from an Ethiopian stalagmite (GM1) that grew intermittently around the last interglacial, which is very pertinent to this discussion. Though it is not a continuous record over the whole period of the last interglacial, the growth phases of GM1 are dated at particularly important periods of the MIS 5. The GM1 record, the oldest high-resolution climate record so far published from Ethiopia and continental eastern Africa, is therefore very significant in an area where any kind of reliable continental climate records from this period are scarce.

These annual-resolution records of  $\delta^{18}\text{O}$ ,  $\delta^{13}\text{C}$ , trace elements and growth rate are from the Goda Mea Cave in Ethiopia (Fig. 1b). A combination of U-Th dates and lamina counting are used to identify the timing of the growth phases. Samples milled at annual

resolution were analysed for  $\delta^{18}\text{O}$  and  $\delta^{13}\text{C}$ , and at decadal resolution for trace elements. Variogram, autocorrelation and spectral analyses of the geochemical and growth rate time series are used to develop a conceptual model for the hydrology of the waters feeding the speleothem. The time series of  $\delta^{18}\text{O}$ ,  $\delta^{13}\text{C}$ , trace elements and annual growth rate are then interpreted, with comparison to the published modern and Holocene stalagmites from the region and globally. Such high resolution, multi-proxy approach has been proved useful in reconstructing annual, in some cases seasonal, rainfall (e.g., Johnson et al., 2006).

## 2. Methodology

### 2.1. Site description

Goda Mea Cave was explored and surveyed in 2007 and a full description can be found in Gunn et al. (2009). The cave is entered from a collapse doline and after about 30 m there is a large flow-stone deposit that almost fills the passage. A crawl beneath opens into a NE-SW oriented rift passage that is initially some 5 m wide by 1 m high but increases downstream to 10–15 m by 7 m. The cave ends in a 90 m x 40 m x 20 m high chamber formed by upwards stoping as evidenced by abundant breakdown. Above the chamber there is ~25 m of sandy limestone intercalated with some thin marl and mudstone layers towards the top, overlain by a ~20 m thick calcareous sandstone, silt, carbonate rich shale and marl intercalation, which extends to ~1 m of soil at the surface. The limestone and sandstone-shale-marl units above the cave form a continuous hydrogeological unit, connected by network of fractures.

There are numerous speleothems in the chamber including stalactites, stalagmites and a central column that is over 10 m high and 6 m diameter. The speleothems are mostly relict with some evidence of re-solution and many of the stalagmites are fractured, most likely by tectonic activity (Fig. 1c and d). Speleothem growth is generally focused along some aligned zones below major fracture systems/brecciated fault traces crossing the hydrogeological unit all the way up to the surface.

Some modern monitoring data (e.g., drip water chemistry) for the cave is presented in Asrat et al. (2008). Drip water  $\text{Ca}^{2+}$  and  $\text{Mg}^{2+}$  concentrations in all analysed drip water samples from this cave are  $2.57 \pm 0.65$  mmol/L and  $1.54 \pm 1.12$  mmol/L, respectively. The drip water  $\text{Ca}^{2+}$  concentration in this cave is high as compared to the range of  $\text{Ca}^{2+}$  in the Mechara caves ( $2.63 \pm 2.36$  mmol/L) and falls within the range of values expected for “open system” evolution (Baker et al., 2016). The high  $\text{Ca}^{2+}$  concentration can be attributed to the open system calcareous sandstone/shale, marl and limestone hydrogeological unit, with the calcite-cemented sandstones, carbonate rich shale, marl and limestone all contributing  $\text{Ca}^{2+}$  ions to the drip waters.

### 2.2. Sample description

GM1 is a large broken stalagmite found in the cave chamber. The 591 mm long stalagmite was sectioned into two halves, and one half polished for lamina counting (Fig. 2). The polished half shows continuous laminations, alternating between dense and porous/white calcite, as well as visually recognizable growth hiatuses,

**Fig. 1.** (a) Regional structural setting of Ethiopia showing the location of Mechara. Lake Tana, and the epicentres of the major earthquakes in the Main Ethiopian Rift and the adjoining highlands are marked (Note that earthquake epicentres in the northern Afar depression are not represented). Insets show the mean position of the ITCZ in July (Boreal summer) and January (winter) over Africa; and the mean monthly rainfall (mm) and mean monthly temperature of the Mechara region, at the Bedesa Meteorological Station (1994–2014 data from the Ethiopian Meteorological Agency). Location of (b) is marked by a broken triangle around the location of Mechara (modified from Asrat et al., 2008); (b) The topography, geology, structure and drainage system of the Mechara karst area and locations of the entrances to the caves mentioned in the text; (c) Goda Mea cave (surveyed according to BCRA Grade 3 using tape, compass and clinometer); (d) a photograph of the main chamber of the Goda Mea cave interior showing the collapse chamber on which grew several speleothems following a major fracture system (photograph by J. Gunn). Figures (a) and (b) modified from Asrat et al. (2008); Fig. (c) modified from Gunn et al. (2009).



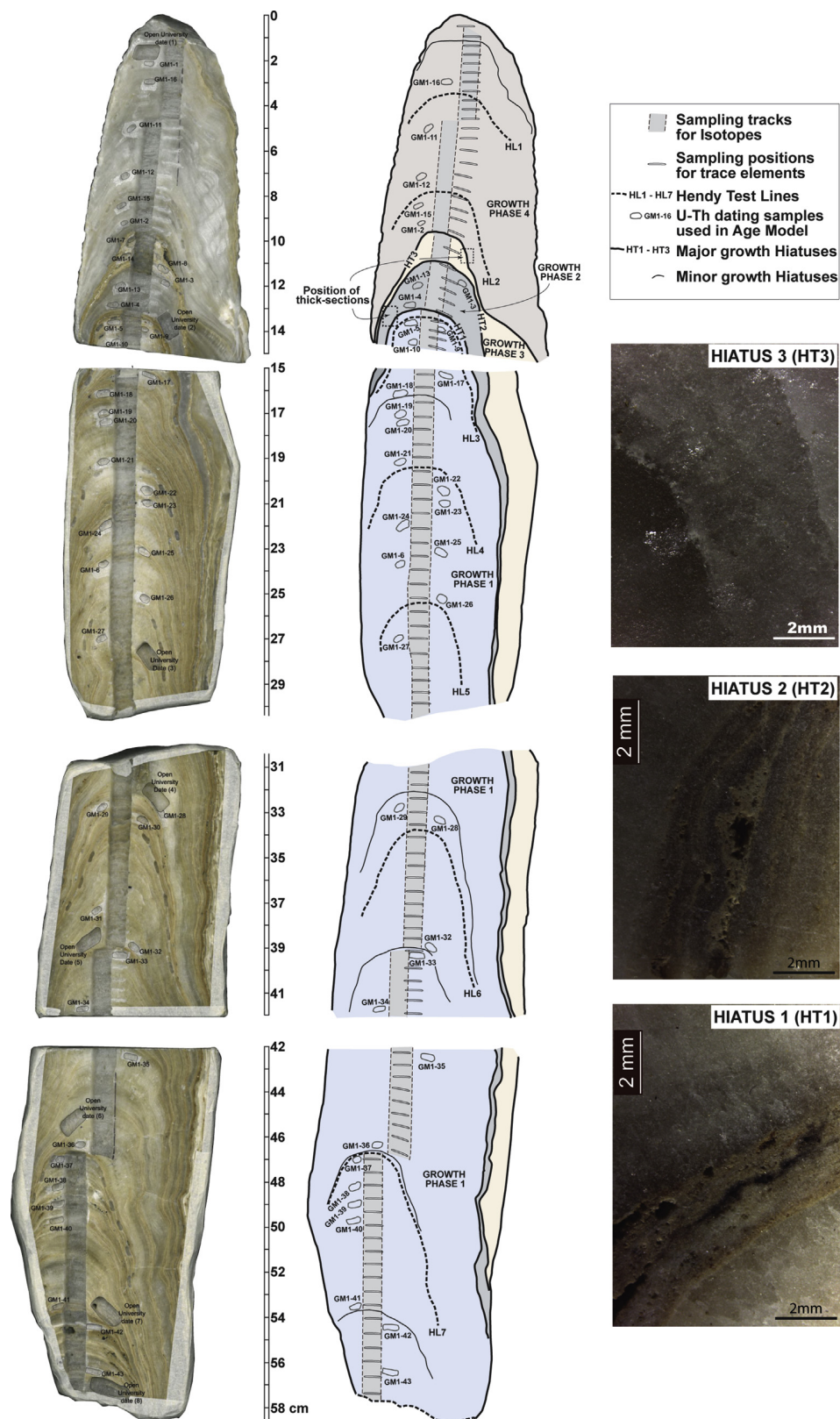


**Fig. 2.** GM1 hand-section in both scanned image (left) and sketch (middle), showing the four major growth phases, locations of the major and minor growth hiatuses, and sampling for isotopes, trace elements and U-Th analyses. Right: photomicrographs of thick sections from across the major growth hiatuses showing a clear evidence of growth stoppage with no apparent dissolution.

marked by shifts in growth axis and the stalagmite morphology. The other half of GM1 was milled using a hand held dental drill for oxygen and carbon isotopes at ~0.6 mm resolution (966 samples), and trace element analysis at ~5.5 mm resolution (103 samples). 38 samples for U-Th dating were similarly drilled using a dental drill, with samples located either side of possible growth hiatuses, and regularly spaced within growth phases.

### 2.3. Geochemical analyses

U-Th analyses were undertaken by ICP-MS at the University of Melbourne, Australia, following the method of [Hellstrom \(2003\)](#). Samples were dissolved in concentrated HNO<sub>3</sub> and equilibrated with a mixed <sup>229</sup>Th–<sup>233</sup>U–<sup>236</sup>U tracer. U and Th were extracted in a single solution using Eichrom TRU resin before introduction to a Nu Plasma multi-collector ICP-MS, where isotope ratios of both elements were measured simultaneously. The decay constants of [Cheng et al. \(2013\)](#) were used, and detritally-corrected ages calculated using eqn. (1) of [Hellstrom \(2006\)](#) with an assumed initial [<sup>230</sup>Th/<sup>232</sup>Th] of 1.5 ± 1.5. Age-depth modelling combined floating annual laminae chronologies and U-Th analyses were as described in section 3.1.

Oxygen and carbon isotopes were analysed at the Stable Isotope Laboratory (SILLA), University of Birmingham, UK. The calcite samples were reacted with phosphoric acid and analysed using an Isoprime continuous flow mass spectrometer. By comparison with a laboratory marble standard, the sample <sup>18</sup>O/<sup>16</sup>O and <sup>13</sup>C/<sup>12</sup>C ratios are reported as δ<sup>18</sup>O and δ<sup>13</sup>C values in per mil (‰) versus VPDB. Analytical precisions are 0.07‰ for δ<sup>18</sup>O and 0.04‰ for δ<sup>13</sup>C on the standard marble (KCM).

Trace elements powders were analysed at University of New South Wales, Sydney. Samples of approximately 0.05 g each were weighed directly into polypropylene vials. One mL of 1–1 hydrochloric acid was added to each vial. The samples were sonicated for 15 min to ensure complete dissolution. The solutions were diluted to 10.0 mL with ASTM<sup>®</sup> Type I water (Millipore<sup>®</sup> filtration system, Millipore<sup>®</sup> Corporation, Billerica, Massachusetts, USA).

Diluted samples were analysed for Ca (317.933 nm) and Mg (285.213 nm) using the PerkinElmer Optima™ 7300DV ICP-OES (PerkinElmer, Shelton, USA). Ba and Sr were analysed by PerkinElmer NexION 300D ICP-MS (PerkinElmer, Shelton, USA). Both instruments were coupled with an ESI SC4 FAST sample introduction system (Elemental Scientific, Inc., Omaha, USA) to minimise sample carryover.

The ICP-OES and ICP-MS were calibrated using certified multi-element standards in a matrix of 2% HCl. Wavelength and analytical mass selection took into consideration spectral interferences as well as sensitivities. Internal standards were added on-line via injection valve to correct for physical interferences. Quality control check standards were run at selected intervals in an unattended automatic analysis run, to ensure that the instrument performance remained consistent over the length of analysis.

### 2.4. Time series analysis

Statistical analysis on the annual growth rate time series followed the approach of [Mariethoz et al. \(2012\)](#), which included the analysis of the first derivative of growth rate (growth acceleration) to determine the flickering parameter (*f*), which is the magnitude of the anti-correlation at lag 1. Flickering ranges between –0.5 and 0, the more negative *f* values indicating stronger flickering. Negative values of *f* are indicative of a karst store filling and draining, as opposed to a climate forcing, and helps identify climatically sensitive speleothems. In addition, variogram analysis of the growth rate time series permits the derivation of the information content

(*IC*) and range (*r*) in the growth rate data, which helps identify the signal: noise ratio in the data and the time over which useful information might be expected. Stable isotope and annual growth rate time series data were also analysed for their autocorrelation and spectral properties. As the data was evenly spaced in time, spectral analysis was performed using discrete Fourier transforms, using the FFTW library within Microcal Origin. Five windows were used (Bartlett, Hanning, Rectangular, Welsh and Triangular) in order to investigate the extent of signal leakage.

## 3. Results

### 3.1. GM-1 chronology

#### 3.1.1. Lamina

Lamina were counted (in duplicate) and a total of 1356 lamina were identified with a mean lamina thickness of 0.44 ± 0.14 mm (ranging between 0.19 and 1.12 mm). This lamina thickness compares well to those reported for stalagmites in previous studies in the region (Ach-1, mean = 0.53 ± 0.26 mm, Bero-1 = 0.45 ± 0.23 mm, Asfa-3 = 0.32 ± 0.11 mm; Merc-1 = 0.29 ± 0.04 mm; [Asrat et al., 2007](#); [Baker et al., 2007](#); [Baker et al., 2010](#)). In these stalagmites, the visible laminae have been demonstrated to be annual by comparison to the radiometric dates. The GM1 laminae are similar in their appearance and thickness to these other stalagmites. Examination of thick sections of GM1 at various levels of the growth phases ([Fig. 2](#)) show continuous and regular visible laminae with alternating brownish calcite (Dark Compact Laminae, DCL) and thinner white calcite (White Porous Laminae, WPL) as defined by [Genty and Quinif \(1996\)](#) and [Genty et al. \(1997\)](#). The presence of fine sediments on the white porous calcite, and some dissolution features at the top of the DCL, suggests some seasonal infiltration variability (*cf.* [Borsato et al., 2007](#)). Overall, the regularly alternating DCL/WPL laminae sequence, even without more obvious structures from infiltration variability, indicate deposition under a seasonal hydroclimate regime (e.g. changes in drip water supersaturation or cave air CO<sub>2</sub> concentration), where recharge was sufficient to maintain continuous dripping to the stalagmite.

#### 3.1.2. Growth hiatuses

There are three major growth hiatuses based on the U-Th chronology (see below), and other possible minor growth hiatuses have been recognized by changes in the growth axis within the growth phases ([Fig. 2](#)). Visual examination of the three major growth hiatuses on the polished stalagmite and the thick sections show that the hiatuses between the four major growth phases are all marked by accumulation of fine detritus and brownish material on the top 2 mm sections, with no indications of dissolution. Such textural features are typical of the ceasing of growth due to cessation of the drip source ([Railsback et al., 2013](#)).

#### 3.1.3. Stalagmite morphology

The morphology of the stalagmite changes from candle stick shaped, with regular nearly horizontal lamina on and off the growth axis for most of the first growth phase to upwards-thinning, laterally less extensive layers with laminae rapidly changing to sub-vertical angle, off the growth axis, just below the first hiatus ([Fig. 2](#)). The second growth phase above the first hiatus then gets broader at its axis with rapid flowing/dripping down the sides of the stalagmite forming nearly vertical lamina. The third growth phase shows similar morphology to the second though it rapidly thins towards the top below the third major hiatus. The last growth phase has relatively broader shape with significant deposition along its axis. The morphology of the stalagmite changing with the hiatus position is a clear demonstration of the changing amount and

concentration of calcite in the dripping water. It shows a general drying out of the drip source towards the tops of the three older growth phases, while the last growth phase is marked by an increased drip rate throughout the growth period.

### 3.1.4. U-Th dates and annual growth rate

The 38 U-Th dates on the sample (Fig. 3, Table 1) demonstrate 4 periods of growth and confirm the presence of 3 hiatuses. Several age inversions are present, and one short growth phase containing 37 laminae was undated.

The U-Th ages were used to constrain a chronology based on the annual laminae. Firstly, the longest phase of speleothem growth (from ~127 mm from the top, to the base at 591 mm) contained 29 very similar U-Th ages (a mean and standard deviation of  $130.0 \pm 3.5$  ka, with an average uncertainty on individual analyses of 1.3 ka), providing further evidence that the 1087 laminae present in this growth phase are likely to be annual. Secondly, following established methods (Asrat et al., 2007; Dominguez-Villars et al., 2012; Baker et al., 2015), we compared two approaches to tie the lamina chronology to the U-Th ages. The first approach was as follows: within each growth phase, each U-Th age was adjusted by using its relative laminae age to obtain an equivalent U-Th age for the date of the start of each growth phase. Taking the mean and standard deviation, this yielded growth phases starting at  $129.3 \pm 2.7$  ka,  $120.7 \pm 1.7$  ka, and  $108.3 \pm 0.2$  ka. We compared this approach to that calculated from linear regression applied to conventional age-depth plots. In this case, we used only the U-Th ages with a  $[^{230}\text{Th}]/[^{232}\text{Th}] > 1000$ , presuming they would be the most accurate. This approach yielded a date for the start of deposition for

two of the four growth phases of  $129.2 \pm 1.7$  ka and  $120.6 \pm 0.3$  ka. The two approaches therefore give consistent dates for the start of deposition that agree with the analytical error of individual analyses.

GM1 deposition periods are therefore ascribed to four phases: 1087 years commencing  $129.3 \pm 2.7$  ka, 54 years of deposition at  $120.7 \pm 1.7$  ka, a 37-yr long undated growth phase, and 176 years of deposition from  $108.4 \pm 0.3$  ka. The ~129.3 ka growth phase occurs, within dating uncertainty, at Termination II or the early part of the last interglacial (Cheng et al., 2009), and the 120.7 ka deposition immediately post-dates the full interglacial. The growth phase at  $108.5$ – $108.3$  ka falls within the isotope stage 5c interglacial.

The annual growth rate for GM1, determined from the annual lamina thickness, is presented in Fig. 4. Mean growth rate does not vary between growth phases:  $0.43 \pm 0.14$  mm/yr (129.3 ka),  $0.41 \pm 0.17$  mm/yr (120.7 ka),  $0.53 \pm 0.15$  (undated), and  $0.47 \pm 0.14$  mm/yr (108.4 ka).

### 3.2. Oxygen and carbon isotopes

The oxygen and carbon isotope ( $\delta^{18}\text{O}$  and  $\delta^{13}\text{C}$ ) data were ascribed to an annual lamina and are presented in Fig. 4. Scatter plots of  $\delta^{18}\text{O}$  and  $\delta^{13}\text{C}$ , including the analysis of the isotopes along a lamina (the 'Hendy test') are shown in Figure S1.

$\delta^{18}\text{O}$  varies significantly between growth phases ( $-7.77 \pm 0.57\text{‰}$  (129.3 ka),  $-3.82 \pm 0.61\text{‰}$  (120.7 ka),  $-6.05 \pm 0.76\text{‰}$  (undated), and  $-6.31 \pm 0.59\text{‰}$  (108.4 ka). Within each growth phase,  $\delta^{18}\text{O}$  can be described as having long periods of relatively invariant composition (e.g.,  $\pm 0.33\text{‰}$  for the first 1000 years of the 129.3 ka

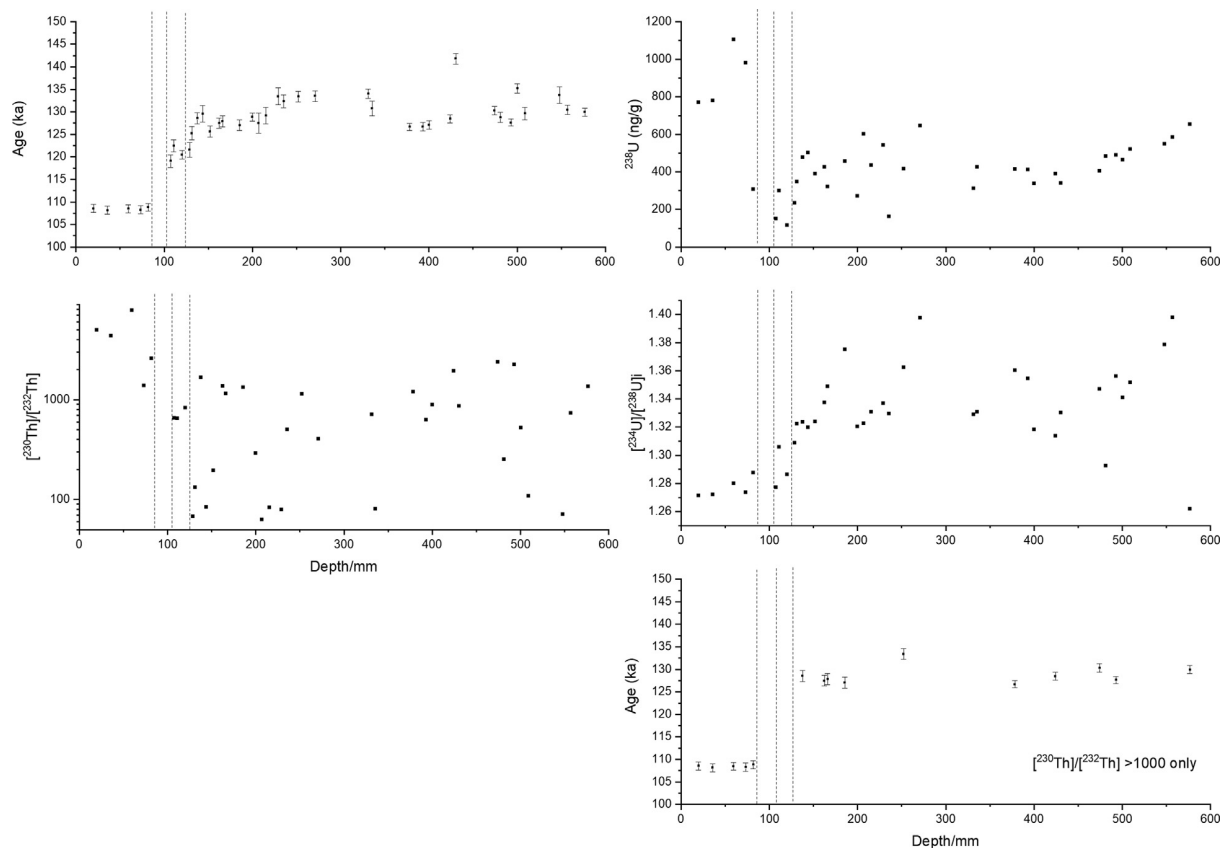


**Fig. 3.** U-Th data for stalagmite GM1. (a) Corrected U-Th ages vs depth for all analyses. (b)  $^{238}\text{U}$  concentration vs depth (c)  $[^{230}\text{Th}]/[^{232}\text{Th}]$  vs depth (d) Initial  $[^{234}\text{U}]/[^{238}\text{U}]$  vs depth (e) U-Th ages vs depth for samples with  $[^{230}\text{Th}]/[^{232}\text{Th}] > 1000$ . In all plots, the three major hiatuses are shown as vertical dashed lines.

**Table 1**  
U and Th isotope data and age determinations (in depth order) for stalagmite GM1. Square brackets indicate activity ratios. Ages shown are corrected for an initial  $^{230}\text{Th}/^{232}\text{Th}$  of 1.5 and a 100% uncertainty, which is incorporated into the age uncertainty.

Sample ID	Distance from top (Midpoint, mm)	Thickness $\pm$ (mm)	Lab Number	Mass (g)	$^{238}\text{U}$ (ng/g)	$2\sigma$	$^{230}\text{Th}/^{238}\text{U}$	95% ext.	$^{234}\text{U}/^{238}\text{U}$	95% ext.	$^{230}\text{Th}/^{232}\text{Th}$	$^{234}\text{U}/^{238}\text{U}$	$2\sigma$	Age (ka)	$2\sigma$
GM1-16	19.88	1.39	UMD130625-303	0.0420	769	58	0.7737	0.0033	1.1998	0.0026	5004.0	1.2716	0.0033	<b>108.556</b>	0.880
GM1-11	35.80	1.02	UMD130301-373	0.0473	779	58	0.7724	0.0031	1.2003	0.0032	4368.7	1.2719	0.0039	<b>108.173</b>	0.890
GM1-12	59.58	1.19	UMD130301-374	0.0458	1105	83	0.7779	0.0028	1.2061	0.0035	7843.4	1.2801	0.0043	<b>108.480</b>	0.866
GM1-15	73.40	1.34	UMD130625-307	0.0490	982	74	0.7739	0.0035	1.2016	0.0025	1389.5	1.2738	0.0031	<b>108.256</b>	0.909
GM1-2	81.85	1.24		0.0183	307	23	0.7832	0.0036	1.2113	0.0019	2604.1	1.2874	0.0024	<b>108.821</b>	0.886
GM1-3	107.35	1.50		0.0189	152	11	0.8160	0.0051	1.1979	0.0028	653.2	1.2771	0.0037	<b>119.049</b>	1.430
GM1-13	110.99	1.07	UMD130410-223	0.0490	301	23	0.8437	0.0046	1.2163	0.0029	651.3	1.3058	0.0038	<b>122.482</b>	1.326
GM1-4	120.32	1.04		0.0245	117	9	0.8261	0.0029	1.2037	0.0028	829.3	1.2864	0.0035	<b>120.516</b>	0.940
GM1-5	128.86	0.89		0.0308	234	18	0.8476	0.0014	1.2190	0.0011	68.1	1.3088	0.0020	<b>121.531</b>	1.634
GM1-9	131.48	0.91	UMD130410-220	0.0340	348	26	0.8648	0.0042	1.2263	0.0030	132.2	1.3224	0.0039	<b>125.265</b>	1.503
GM1-10	137.62	1.24	UMD130301-368	0.0333	480	36	0.8734	0.0038	1.2250	0.0035	1670.8	1.3236	0.0044	<b>128.556</b>	1.258
GM1-17	143.71	1.67	UMD130301-383	0.0453	503	38	0.8791	0.0036	1.2218	0.0033	84.4	1.3198	0.0043	<b>129.587</b>	1.796
GM1-18	152.18	1.24	UMD130410-235	0.0420	391	29	0.8657	0.0036	1.2271	0.0028	196.2	1.3239	0.0036	<b>125.587</b>	1.246
GM1-19	162.38	1.05	UMD130301-386	0.0455	427	32	0.8778	0.0036	1.2355	0.0032	1366.1	1.3376	0.0041	<b>127.491</b>	1.167
GM1-20	166.11	1.01	UMD130410-248	0.0380	321	24	0.8854	0.0040	1.2430	0.0032	1155.9	1.3488	0.0040	<b>127.878</b>	1.239
GM1-21	185.52	1.31	UMD130301-419	0.0445	458	34	0.8973	0.0039	1.2619	0.0035	1335.6	1.3750	0.0043	<b>127.047</b>	1.222
GM1-22	200.09	1.51	UMD130821-554	0.0440	272	20	0.8737	0.0023	1.2226	0.0023	290.9	1.3204	0.0029	<b>128.860</b>	0.874
GM1-23	207.12	1.18	UMD130301-506	0.0432	603	45	0.8758	0.0039	1.2251	0.0038	63.2	1.3227	0.0050	<b>127.504</b>	2.214
GM1-24	215.50	1.12	UMD130410-249	0.0400	436	33	0.8840	0.0042	1.2296	0.0030	83.4	1.3308	0.0041	<b>129.161</b>	1.837
GM1-25	229.21	1.23	UMD130301-512	0.0364	542	41	0.9011	0.0036	1.2311	0.0033	79.4	1.3370	0.0044	<b>133.450</b>	1.894
GM1-6	235.62	1.25		0.0373	162	12	0.8893	0.0041	1.2268	0.0036	500.7	1.3297	0.0046	<b>132.346</b>	1.406
GM1-26	252.24	1.48	UMD130410-257	0.0400	417	31	0.9106	0.0036	1.2486	0.0030	1146.6	1.3624	0.0038	<b>133.387</b>	1.193
GM1-27	271.04	1.36	UMD130301-530	0.0428	647	49	0.9315	0.0032	1.2727	0.0034	405.0	1.3976	0.0043	<b>133.482</b>	1.154
GM1-29	331.42	1.34	UMD130826-251	0.0399	313	23	0.8938	0.0032	1.2252	0.0023	709.8	1.3289	0.0030	<b>134.011</b>	1.058
GM1-30	335.76	1.14	UMD130826-256	0.0411	426	32	0.8892	0.0028	1.2287	0.0023	81.0	1.3310	0.0032	<b>130.740</b>	1.657
GM1-31	378.25	1.23	UMD130826-292	0.0417	414	31	0.8879	0.0025	1.2519	0.0021	1197.3	1.3603	0.0027	<b>126.688</b>	0.785
GM1-32	393.31	1.30	UMD130826-294	0.0479	412	31	0.8850	0.0032	1.2479	0.0021	626.9	1.3546	0.0027	<b>126.679</b>	0.947
GM1-33	400.31	1.20	UMD130826-296	0.0454	338	25	0.8659	0.0030	1.2221	0.0022	894.0	1.3181	0.0028	<b>127.130</b>	0.938
GM1-34	424.23	1.35	UMD130826-299	0.0440	391	29	0.8676	0.0023	1.2183	0.0029	1954.1	1.3139	0.0036	<b>128.468</b>	0.885
GM1-35	430.55	1.45	UMD130826-311	0.0477	340	26	0.9170	0.0032	1.2211	0.0025	862.6	1.3301	0.0032	<b>141.786</b>	1.166
GM1-36	474.48	1.73	UMD130826-343	0.0466	405	30	0.8921	0.0029	1.2402	0.0024	2385.8	1.3471	0.0030	<b>130.298</b>	0.940
GM1-37	481.18	1.46	UMD130826-347	0.0443	482	36	0.8580	0.0030	1.2033	0.0027	252.3	1.2925	0.0035	<b>128.774</b>	1.122
GM1-38	493.04	1.09	UMD130826-349	0.0492	489	37	0.8884	0.0025	1.2482	0.0020	2242.0	1.3560	0.0025	<b>127.627</b>	0.777
GM1-39	500.38	1.27	UMD130826-352	0.0685	465	35	0.9045	0.0030	1.2327	0.0023	525.1	1.3410	0.0030	<b>135.228</b>	1.030
GM1-40	508.89	1.02	UMD130826-356	0.0517	520	39	0.8962	0.0028	1.2438	0.0027	108.8	1.3517	0.0036	<b>129.654</b>	1.373
GM1-41	547.95	1.23	UMD130826-365	0.0414	550	41	0.9262	0.0027	1.2594	0.0025	71.7	1.3785	0.0036	<b>133.740</b>	1.816
GM1-42	557.20	1.59	UMD130826-380	0.0463	585	44	0.9216	0.0035	1.2751	0.0025	731.2	1.3978	0.0032	<b>130.485</b>	1.060
GM1-43	576.75	1.25	UMD130826-414	0.0495	654	49	0.8432	0.0024	1.1814	0.0025	1362.5	1.2619	0.0032	<b>129.948</b>	0.890



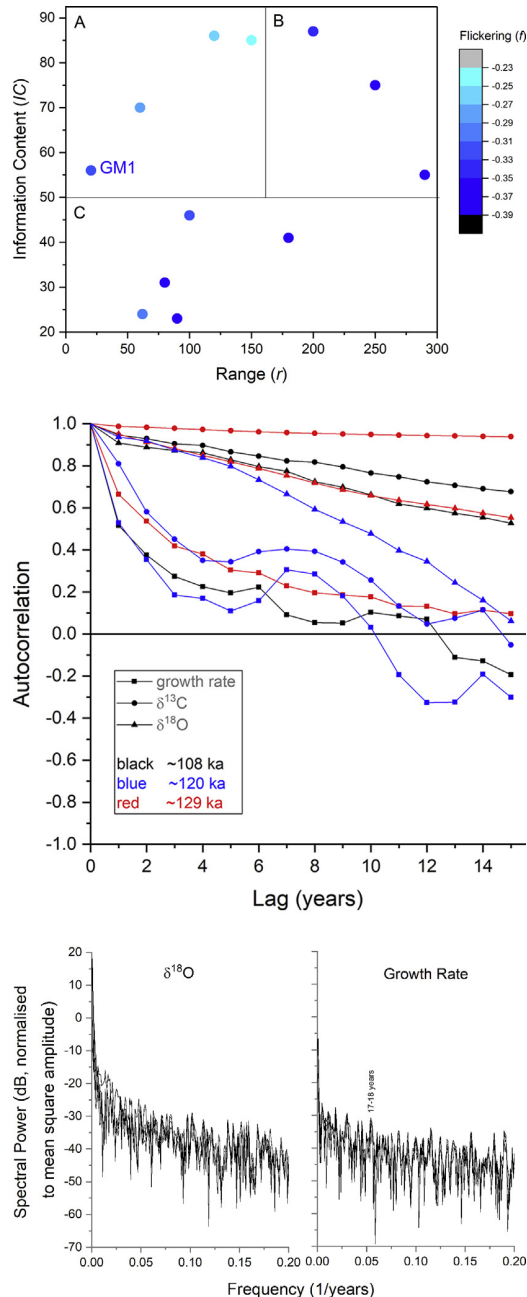


**Fig. 4.** GM1 times series for the geochemical proxies. From top: growth rate,  $\delta^{13}\text{C}$ ,  $\delta^{18}\text{O}$ , Sr/Ca, Mg/Ca, Ba, Ca. Note the axis breaks on the x-axis, which permit equal scaling of data on the time axis.

deposition period, and  $\pm 0.23\text{‰}$  in the first 150 years of the 108.4 ka deposition period), as well as periods of rapid change. For example,  $\delta^{18}\text{O}$  increased from  $-7.8\text{‰}$  to  $-5.3\text{‰}$  in four years (and to  $-4.5\text{‰}$  after 13 years) at the end of the 129.3 ka growth phase, and from  $-6.2\text{‰}$  to  $-4.4\text{‰}$  in 9 years at the end of the 108.4 ka growth period.

$\delta^{13}\text{C}$  is characterised by low inter-sample variability, with the presence of long-term trends. For example, in the 129.3 ka growth phase, the standard deviation of  $\delta^{13}\text{C}$  over any 50-year period is between 0.1‰ and 0.3‰, but over the whole 1087 years of deposition,  $\delta^{13}\text{C}$  trends from  $-1\text{‰}$  to  $-4\text{‰}$ . This 3‰ change in  $\delta^{13}\text{C}$  with the growth phase is as great as the variability between growth

phases.

Figure S1 shows the relationship between  $\delta^{18}\text{O}$  and  $\delta^{13}\text{C}$ , both throughout the time series as well as along growth layers ('Hendy tests'). The Hendy tests suggest a 1‰ increase or decrease in isotope composition is possible along a growth layer, which is greater than the inter-annual variability of  $\delta^{13}\text{C}$  and  $\delta^{18}\text{O}$ . For stalagmite GM1, there is no evidence for near-equilibrium deposition: modern and Holocene stalagmites demonstrate isotope fractionation of 1–2‰ (Asrat et al., 2007; Baker et al., 2007, 2010), and similar deposition conditions appear to apply to stalagmite GM1. Based on these works, we have quantified these fractionation processes and confirmed that they operate in the same direction as the climate forcing, which has also been observed by other works (e.g., Dorale and Liu, 2009).

### 3.3. Trace elements

Ba/Ca, Mg/Ca and Sr/Ca show similar patterns to  $\delta^{13}\text{C}$  and  $\delta^{18}\text{O}$ , although sampled at a lower temporal resolution. A long-term trend to lower ratios in the 129.3 ka growth phase matches that observed in  $\delta^{13}\text{C}$ . Significant short-term changes in trace element composition occurs at the same time as the increases in  $\delta^{18}\text{O}$  and  $\delta^{13}\text{C}$  at the end of the 129.3 ka growth phase, and within the 120.7 ka growth period. At the end of the 129.3 ka growth phase, a change in gradient of Mg/Ca, Sr/Ca and Ba/Ca lasted for ~170 years, indicative of a drying trend. This was followed by the  $\delta^{18}\text{O}$  increase of 2.2‰ that occurred over 4 years, and then an increased variability in Sr/Ca, Mg/Ca and Ba/Ca (Mg/Ca increases, Mg/Ca and Ba/Ca decrease) until growth stops 28 years later. In contrast, the trace element response at the time of a 2‰ increase in  $\delta^{18}\text{O}$  at the end of the 108.4 ka growth phase is muted and trends to lower values. The greatest range in trace elements occurs in the 120.7 ka growth phase, where Sr/Ca increases, and Mg/Ca and Ba/Ca have opposing increasing and decreasing trends.

### 3.4. Time series analysis on stable isotope and growth rate time-series

Following Mariethoz et al. (2012), and as described in section 2.4, the growth rate time series variogram properties was investigated. Due to the short duration of several of the growth phases, only the longest time series at 129.3 ka was analysed. The results are plotted in Fig. 5a, where variogram analysis on stalagmite GM1 is compared to previous published stalagmite statistics on growth rate series. The autocorrelation and spectral properties of the growth rate,  $\delta^{18}\text{O}$  and  $\delta^{13}\text{C}$  series were also investigated (Fig. 5b and c).

Stalagmite GM1 growth at 129.3 ka has evidence of 'flickering' ( $f = -0.33$ ), that is a growth acceleration that flickers around a mean value (Mariethoz et al., 2012). 'Flickering' has been explained as growth rate sensitivity to the filling and draining of a karst store, which is trying to reach a dynamic equilibrium, with reported values between  $-0.24$  (low flickering, potential climate signal) and  $-0.39$  (high flickering, potential karst hydrology signal).

Variogram analysis shows that the stalagmite has low range ( $r$ , 20.5 years) in the growth rate record. Growth rate therefore has no 'memory' of previous growth rates longer than this timescale, indicative that the karst store(s) that feed the stalagmite are relatively small. The GM1 range is the lowest reported to date for an annually laminated speleothem. The Information Content (IC) of growth rate, which is the balance of the signal in the variogram and the noise, is 56%, indicating that the stalagmite growth rate record contains a greater proportion of signal than noise. In comparison to previously published records (Fig. 5a), stalagmite growth rate statistical properties lie in region A, with stalagmites that have a high



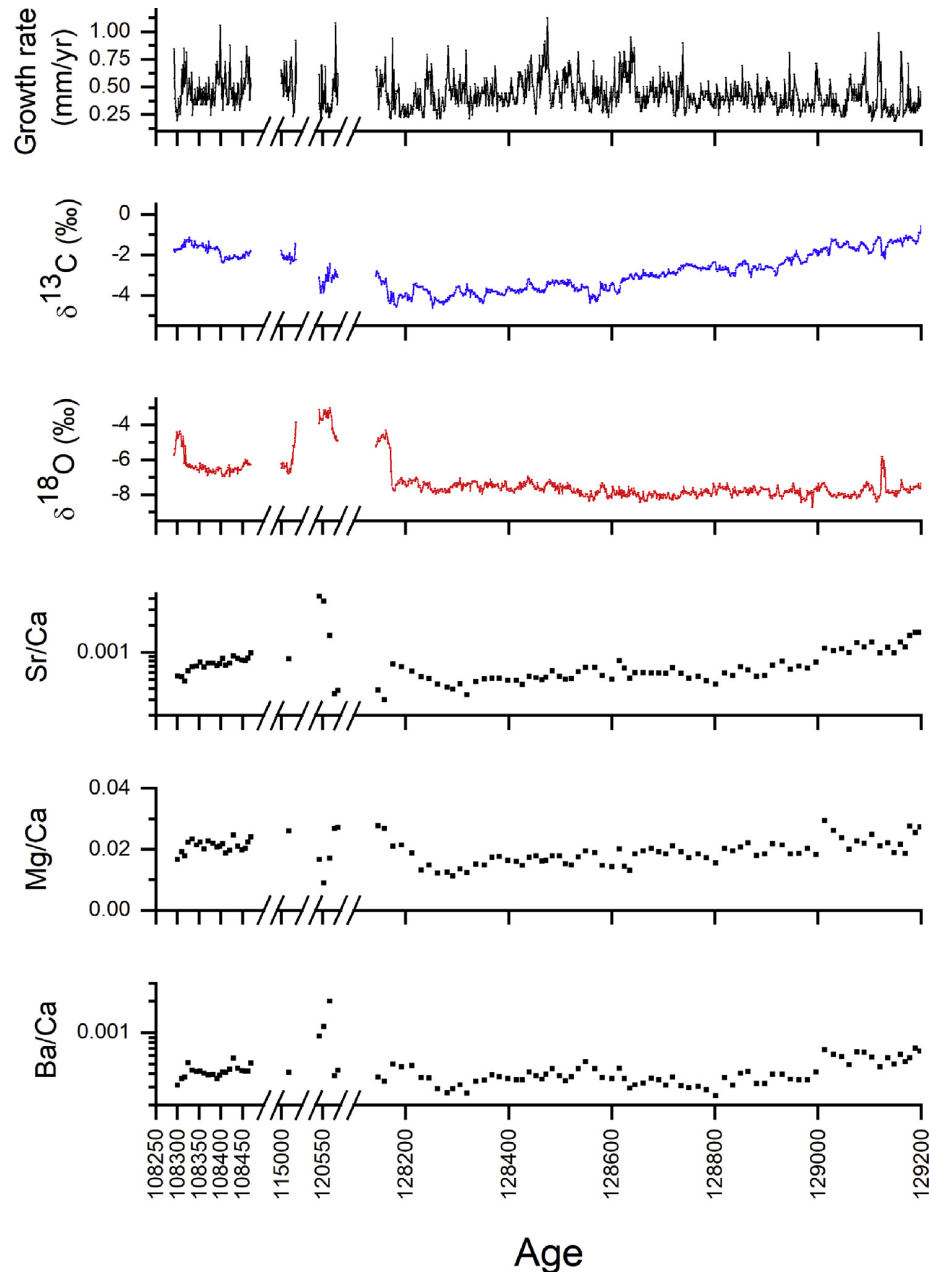


**Fig. 5.** (a) Scatterplot of variogram parameters range, information content and flickering for the 129.3 ka growth phase; (b) Autocorrelation of growth rate,  $\delta^{13}\text{C}$  and  $\delta^{18}\text{O}$  time series for the three U-Th dated growth phases; (c) Spectral analysis on the growth rate and  $\delta^{18}\text{O}$  times series for the 129.3 ka growth phase. The 17–18 years peak, though statistically not significant is marked.

information content, relatively low flickering and range, and where growth rate has proven useful in paleoclimate reconstruction.

Autocorrelation of growth rate,  $\delta^{13}\text{C}$  and  $\delta^{18}\text{O}$  time series are presented in Fig. 5b for the three longest growth phases (~129, ~120 and ~108 ka). Significant autocorrelation can be observed for  $\delta^{13}\text{C}$  and  $\delta^{18}\text{O}$  for the ~129 and ~108 ka growth phases, with autocorrelation  $>0.6$  at 15-year lag. Autocorrelation for  $\delta^{13}\text{C}$  is stronger than for  $\delta^{18}\text{O}$ , indicative of additional smoothing of the  $\delta^{13}\text{C}$ , likely from the soil carbon store. Growth rate has very low autocorrelation ( $<0.4$  after 4 years lag), in agreement with the observed flickering of growth rate. The ~120 ka growth phase has lower autocorrelation of  $\delta^{18}\text{O}$  and  $\delta^{13}\text{C}$  than the other two growth phases, suggesting limited mixing or smoothing of these proxies

during this short growth phase. Low autocorrelation would agree with the observed highest variability in trace elements at this time.

Spectral analysis was also undertaken (Fig. 5c) for the longest continuous growth phase at ~129 ka. Bartlett, Hanning, Rectangular, Welsh and Triangular windows were used to explore the spectral properties for  $\delta^{18}\text{O}$  and growth rate time series. Growth rate has a 17–18 year peak that is not statistically significant at 95% confidence, and two other peaks (31–33 and 53–59 years), which are longer than the range ( $r$ , 20.5 years) and are likely to be harmonics of the 17–18 year frequency.  $\delta^{18}\text{O}$  also has only weak and insignificant spectral power, not surprising given the low variability in the  $\delta^{18}\text{O}$  data.

## 4. Discussion

### 4.1. Holocene stalagmite records

Previous cave research in Ethiopia has included limited cave drip water and climate monitoring during sampling expeditions to the Mechara region of Ethiopia between 2004 and 2008 (Asrat et al., 2008) (Fig. 1), and the analysis of modern and Holocene stalagmite samples. Modern calibration studies of stalagmite  $\delta^{18}\text{O}$  of carbonate shows evidence of climate sensitivity, despite deposition out-of-equilibrium (Baker et al., 2007, 2010). The latter is potentially due to both rapid degassing and evaporation.  $\delta^{18}\text{O}$  and growth rate correlations with climate are sample-specific. Drip-specific flow-paths determine whether a stalagmite has a proxy which is sensitive to the 'big' rains, or to the relative amount of rain in the 'big' and 'small' rain seasons, or neither. For example, modern stalagmite  $\delta^{18}\text{O}$  and growth rate records were reported from two stalagmites from Rukiesia Cave (Baker et al., 2007). The annual nature of the laminae was confirmed by  $^{14}\text{C}$  analyses and comparison to the modern atmospheric bomb carbon peak. In these samples  $\delta^{18}\text{O}$  and growth rate were shown to have a correlation with the ratio of 'small' to 'big' rainfall and total summer rainfall, respectively. A sample specific climate sensitivity of  $\delta^{18}\text{O}$  and growth rate was observed, which probably reflects the karst hydrogeology and its effect on individual water flow-paths. A loss of climate correlation was also observed in one sample during a period of high growth rates.

$\delta^{18}\text{O}$  and growth rate time-series both exhibit multi-decadal variability in two stalagmite samples deposited in the Holocene. Such variability may be an amplification of extremes in hydro-climate (e.g., drought years) or rainfall isotopic composition, due to the non-linear replenishment or drainage of karst stores (Baker et al., 2013). A mid-Holocene record from Achere Cave (sample Ach-1) had laminae that were demonstrated to be annual by comparison to U-Th dates (Asrat et al., 2007). In this stalagmite a 18–21 yr periodicity in growth rate and  $\delta^{18}\text{O}$  occur.  $\delta^{18}\text{O}$  has a greater variability than  $\delta^{13}\text{C}$ , indicative of the variability being driven by variations in the extent of evaporative enrichment of  $\delta^{18}\text{O}$ . A discontinuous Holocene record from Bero Cave had six growth phases over the last 7800 years (Baker et al., 2010). Mean stalagmite  $\delta^{18}\text{O}$  is 1.2‰ higher than that predicted by forward modelling, and a multi-decadal variability in  $\delta^{18}\text{O}$  and growth rate was again observed (Baker et al., 2010).  $\delta^{18}\text{O}$  from this stalagmite was indicative of both rapid degassing and the additional

enrichment, probably due to evaporation.

Stalagmite growth phases are relatively short ( $10^3$ – $10^4$  years) due to the tectonically active nature of the region, which can change water flow paths. This is observed in stalagmites from all three caves, and has been explained by changes in flow regime or to the relative position of a growing stalagmite caused by tectonic activity related to the East African Rift (Asrat, 2012). Physically anomalous laminae within an otherwise regular and visible annual laminae sequence, frequent deviations from vertical growth axis, and abrupt changes in stalagmite morphology, as well as the tectonically-controlled formation of the larger cave system, further confirm the influence of tectonics and recorded earthquakes in the region (see Fig. 1a) on the length of the growth phases (Asrat et al., 2008; Asrat, 2012).

### 4.2. Conceptual growth model

The combination of stable isotope and trace element geochemistry, growth rate, statistical analyses, and observations of the laminae types and stalagmite shape, allow us to build a conceptual model for stalagmite GM1 (Fig. 6).

Firstly, the stalagmite probably had continuous deposition for more than 1000 years, and during this period isotope and trace element composition has low variability and high autocorrelation. This homogeneity of  $\delta^{13}\text{C}$ ,  $\delta^{18}\text{O}$  and trace elements suggests a drip water source which is well mixed, enough to obscure any annual to decadal scale variability in  $\delta^{18}\text{O}$  and maintain dripping. The continuous deposition of the laminae and the candle-stick shape of the stalagmite before it narrows down towards the tip of this growth phase (the last few years of growth) supports a continuous drip source. We propose this water comes from matrix flow of the porous sandstone and sandy limestone, which was channelled to the drip source by a network of small fractures. The annual laminae are driven by this flow regime, which provides the necessary seasonal variability in drip water hydro-geochemistry. Combined with the evidence from flickering, we infer the variations in lamina thickness are driven by the karst hydrology and not by the cave environment. In the ~129 ka growth phase, these would have to maintain high levels of saturation for the initial ~1000 years of deposition.

Secondly, the four growth phases of GM1 reflect the changing karst hydrologic regime above the cave. The ~129 ka growth phase is marked by the dominance of a continuous supply of water from 'matrix' flow for most of its growth period, which rapidly dried out

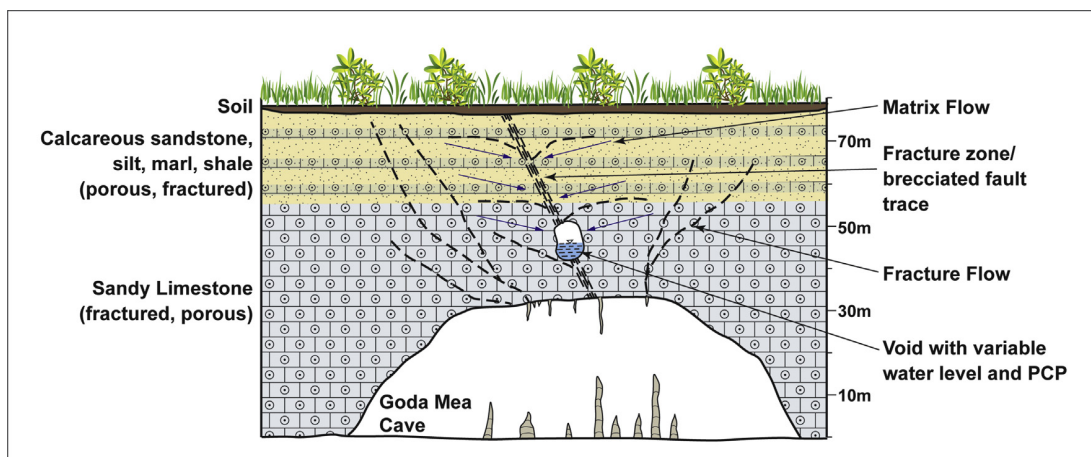


Fig. 6. Conceptual model for the deposition of stalagmite GM1.

a few tens of years before the hiatus. In contrast, the ~120 ka growth phase reflects a rapid ‘fracture’ flow, following a possible tectonic event, which did not maintain growth for a long time before it abruptly shut off as marked by the rapid increase in trace element ratios and  $\delta^{18}\text{O}$ . The third, undated growth phase shows similar features to that of the second, only the growth period was shorter suggesting a rapid start to dripping and subsequent exhaustion from a ‘fracture’ source, as marked by the nearly vertical laminae down the sides of the stalagmite and the abrupt narrowing towards its top. The ~108 ka growth phase is again marked by a more ‘porous’ matrix flow which maintained growth for longer period, attested by the regular laminae, broad stalagmite shape, generally low variability trace element ratios and depleted  $\delta^{18}\text{O}$ .

Thirdly, growth rate varies annually, shows evidence of flickering, and has a range of ~20 years and a spectral peak at 17–18 years. Given the relative homogeneity of the stable isotope and trace element signals, the growth rate variability has to occur subsequent to the mixing of the water. Dissolutionally-enlarged fractures or a network of small conduits would allow limited water storage, permitting degassing of karst water and prior calcite precipitation (PCP) as well as drip rate variations, both affecting growth rate variability. We conceive this store to have a proportional volume of approximately 20 years of recharge (see later). In drying conditions, water from this store could maintain dripping and deposition for short time periods.

Fourth, a pre-existing fracture zone/brecciated fault trace which might have been reactivated during subsequent tectonic activities, extending from the surface, through to the store and the cave roof, permits fracture flow to stalagmite GM1. This would permit short-duration recharge, probably after high magnitude /frequency rainfall events, in the absence of saturated porous sandstone and limestone aquifer. This would explain the short duration, high geochemical variability, ~120 ka growth phase. The absence of ‘stored’ water and subsequently rapid exhaustion of the fracture flow/drip source is supported by the nearly vertical laminae depositing down the sides of the stalagmite, high variability/rapid increase in the  $\delta^{18}\text{O}$  and trace element ratios and low autocorrelation in  $\delta^{13}\text{C}$  and  $\delta^{18}\text{O}$ .

The varying trends between the  $\delta^{18}\text{O}$  and  $\delta^{13}\text{C}$ , and trace element ratios from one growth phase to the other suggests that a single kinetic fractionation process does not dominate our proxy records, rather we infer a hydrological control based on climatic and tectonic processes.

Our conceptual model explains other features of GM1 geochemistry and growth rate. The geochemistry at the end of the 129.3 ka growth phase can be interpreted as a decline in the saturation or water level in the porous media, leading to an increase in  $\delta^{18}\text{O}$  and trace elements as dripping is maintained just from the smaller store. Before growth stops, a change in gradient of Mg/Ca, Sr/Ca and Ba/Ca indicates a drying trend which lasts for ~170 years, followed by a  $\delta^{18}\text{O}$  increase of 2.2‰ that occurred over 4 years, and then increased variability in Sr/Ca, Mg/Ca and Ba/Ca until deposition stops 28 years later. Many of the previously studied stalagmites from Ethiopia such as Ach-1 (Asrat et al., 2007) show similar features, which could be attributed to the specific geological setting of the region where earthquake/tectonics play a strong role in shifting the relative position or the extent of the major ‘fracture’ flow routes for such short-phased growths, leading to growth maintained for short time longer from the smaller ‘matrix’ flow.

The similarity in values for the range  $r$  (20.5 yrs), the spectral frequency  $f$  (17–18 yrs), and the observation that it takes 24 yrs for the stalagmite to stop growing, all suggest the presence of a water store that can hold ~20 years of recharged water. The multi-decadal growth rate frequency of 17–18 yrs, although insignificant, is in agreement with that observed from Holocene stalagmites in the

region (Ach-1, Bero-1; Baker et al., 2010), and similar to observed variability in the modern rainfall pattern and subsequent flow at the upper Blue Nile (Taye and Willems, 2012). Plausible climatic forcing over this timescale includes changes in Atlantic and Indian Ocean sea surface temperature and variability in the movement and intensity of the ITCZ and its effect on Ethiopian rainfall (Degefu et al., 2017). However, the similarity of  $f$  and  $r$  suggests that any climate forcing in GM1 growth rate variability may be amplified by the size of karst water store, or be karstic rather than climatic, the latter something previously observed in forward modelling studies (Baker et al., 2013).

Finally, the shift to higher isotope values within a growth phase can be explained by our conceptual model as a change from porous flow being the dominant water source to a dominance of fracture flow. It suggests that the observed 2‰ shift could be indicative of a water that has undergone additional kinetic or evaporative isotope fractionation. Both fractionation processes had been previously inferred as occurring in both Modern and Holocene Ethiopian speleothems, and from ‘Hendy tests’ on GM1, to a similar extent (up to 1‰). The implication for the climatic interpretation of stalagmite  $\delta^{18}\text{O}$  is that variability of up to 2‰ cannot be directly ascribed to climatic forcing, but larger changes cannot be explained by fractionation processes. Similar rapid shifts in  $\delta^{18}\text{O}$  of +2‰ within a period of 6 years have been identified in the Hulu cave speleothems (Treble et al., 2007).

#### 4.3. The climate record

We can compare the  $\delta^{18}\text{O}$  composition for each GM1 growth phase with published Holocene stalagmite data from Ethiopia (Asrat et al., 2007; Baker et al., 2007, 2010), as well as the modelled solar insolation for 15°N (Laskar et al., 2004), and other archived speleothem  $\delta^{18}\text{O}$  records along the monsoon path and the “downstream” countries (China, Cheng et al., 2016; Israel, Bar Matthews et al., 1999, 2003). This comparison is shown in Fig. 7. In GM-1 the  $\delta^{18}\text{O}$  composition ( $-7.77 \pm 0.57\text{‰}$  (129.3 ka),  $-3.82 \pm 0.61\text{‰}$  (120.7 ka),  $-6.05 \pm 0.76\text{‰}$  (undated), and  $-6.31 \pm 0.59\text{‰}$  (108.4 ka)) is generally isotopically more negative compared to both modern (Merc-1:  $-1.22 \pm 0.31\text{‰}$ ; Asfa-3:  $-1.37 \pm 0.37\text{‰}$ ; Baker et al., 2007), and Holocene (Bero-1:  $-3.42 \pm 1.45\text{‰}$ , Baker et al., 2010; Ach-1:  $-3.20 \pm 0.35\text{‰}$ , Asrat et al., 2007) samples from the region. Even allowing for kinetic fractionation and non-equilibrium deposition of up to 2‰ in all samples, GM1  $\delta^{18}\text{O}$  composition at 129.3 ka, 108.4 ka, and an undated growth phase, is more negative than any Holocene stalagmites from the region. Combined with our conceptual understanding of GM1 deposition, we can be certain that these growth phases and lower isotope composition are indicative of wetter conditions and sustained recharge.

The GM1 record is the first high-resolution last interglacial continental climate record and among the few climate records of any resolution from Ethiopia so far published. A deep seismic and near-continuous core record of the last 150,000 years from Lake Tana on the Northwestern Ethiopian highlands used geochemical proxies (sediment Ca/Ti ratio) for climate-driven lake level fluctuations (Lamb et al., 2018). The oldest cave sediment records from the Southeastern Ethiopian highlands goes back only to  $63 \pm 7$  ka (Tribolo et al., 2017).

The four phases of the GM1 record are dated at particularly important periods of the last interglacial. Noting the quantified age uncertainties (see section 3.1.4), they provide high resolution snapshots from some critical time-windows. The two long growth phases at ~129 ka and ~108 ka, which we conceptualise as being dominated by a sustained porous/matrix flow regime, match maximum summer insolation at 15°N. This suggests that though

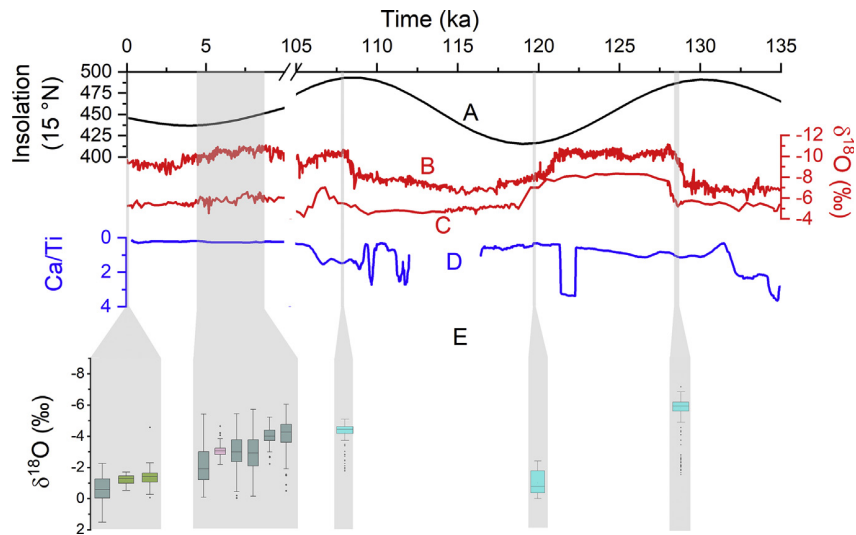


**Fig. 7.** Comparison of climate proxy records. (a) Insolation at 15°N (Laskar et al., 2004); (b) Chinese composite stalagmite  $\delta^{18}\text{O}$  record (Cheng et al., 2016); (c) Soreq Cave  $\delta^{18}\text{O}$  record (Bar-Matthews et al., 1999, 2003); (d) Lake Tana sediment Ca/Ti record (Lamb et al., 2018); (e) Ethiopian stalagmite  $\delta^{18}\text{O}$  composite. Box-plots show median, inter-quartile range and range for each stalagmite; shading represents different caves (grey – Bero Cave; Green – Rukiesia Cave; Orange – Achere Cave; Cyan – Goda Mea Cave). Note the x-axis break; vertical shading aligns the Ethiopian records to the other time series. (For interpretation of the references to colour in this figure legend, the reader is referred to the Web version of this article.)

internal growth variability may be dominated by karst hydrology above the cave, the GM1 growth as a whole and the geochemical proxies were responding to climate forcing.

Comparison of the GM1  $\delta^{18}\text{O}$  record with the China composite  $\delta^{18}\text{O}$  record (Hulu and Dongge caves; Cheng et al., 2016), the Soreq cave (Israel)  $\delta^{18}\text{O}$  record (Bar-Matthews et al., 1999, 2003) (Fig. 7) suggests a similar relationship for all three sites, with wet conditions (lower  $\delta^{18}\text{O}$  and peak summer insolation) during the ~108 ka growth period, and dry or drying conditions (higher  $\delta^{18}\text{O}$  and low summer insolation) at the ~120 ka growth period. The Soreq cave  $\delta^{18}\text{O}$  record from central Israel in the Levant has been shown to indicate enhanced rainfall (Bar-Matthews et al., 1999) and could be a “downstream” indicator of a stronger northeast African monsoon (Tierney et al., 2017). At ~129 ka, the lower  $\delta^{18}\text{O}$  and wetter conditions in Ethiopia occur at the summer insolation maxima, but may occur before the isotope response observed in Israel and China. Dating uncertainty in the GM1 record prevents a more precise interpretation, but it does raise the possibility of the intensification of the East African Monsoon before other northern hemisphere monsoon systems at the start of the last interglacial. The Lake Tana (Northwestern Ethiopian highlands) sediment Ca/Ti record (Fig. 7) indicates an abrupt increase in moisture even earlier at ~132 ka, leading to stable high lake level conditions during the period ~132 ka to ~95 ka, with some brief dry episodes (Lamb et al., 2018). This period is defined by a generally flat trend of Ca/Ti, truncated by very brief high Ca/Ti excursions. The major wet conditions during the ~129 ka and 108 ka growth phases of GM1 are generally consistent with this predominantly high lake level phase, although they do not particularly correspond to the lowest values of Ca/Ti.

As speleothem records of the Holocene from the region (Fleitmann et al., 2007) show, decreasing  $\delta^{18}\text{O}$  values during the early Holocene indicate a rapid northward migration of the summer ITCZ and intensification of the rain belt of the Indian Summer Monsoon. On the other hand, the southward migration of the ITCZ during the middle to late Holocene, marked by increasing  $\delta^{18}\text{O}$  values in speleothems, led to weakening of the associated summer monsoon. Similar studies from Madagascar (e.g., Voarintsoa et al., 2017) have also shown the link between speleothem  $\delta^{18}\text{O}$  values and the ITCZ migration. The ~129 ka growth phase of GM1 could

therefore be effectively considered as an annual record of relative ITCZ position ~129 ka BP.

Ethiopia/northeast Africa has been considered as the origin of Anatomically Modern Humans (White et al., 2003; McDougall et al., 2005) and possibly the region out of which Anatomically Modern Humans dispersed during MIS 5–3 or during earlier migration episodes (cf. Hershkovitz et al., 2018). Considering the significant debate about the role climate variability played in human evolution and dispersal of Anatomically Modern Humans “Out of Africa” (e.g., Tierney et al., 2017 and references therein; Lamb et al., 2018), high-resolution speleothem records from Ethiopia and northeastern Africa such as those of GM1 can shed light on this debate. The GM1 record for instance shows that the earliest human migration during MIS 5, confirmed by the presence of ~110–80 ka old Anatomically Modern Human fossils in Israel (Grün et al., 2005), occurred during a major wet event in northeast Africa. The Tana Lake record confirms that the northwestern Ethiopian highlands experienced relatively stable moist climate during MIS 5c–e (Lamb et al., 2018). This supports earlier conclusions that human migration occurred during humid conditions, as such conditions provided humans “green corridors” to overcome inhospitable deserts (e.g., Timmerman and Friedrich, 2016). However, the major episode of human migration occurred during 50–75 ka (Nielsen et al., 2017), and marine records from the Gulf of Aden show that this migration event occurred during a sustained dry condition in northeast Africa (Tierney et al., 2017), while the Lake Tana record shows more complex climate variability during this period (Lamb et al., 2018). Future research is required on the speleothems from Goda Mea and Aynage caves, some of which have been dated to the critical period of 120–50 ka.

## 5. Conclusions

Stalagmite GM1 was deposited discontinuously around the time of the last interglacial, at ~129 ka, 120 ka, an undated growth phase, and ~108 ka. Variogram analysis of growth rate shows a low range (20.5 years), some flickering (−0.33) and good information content (56%), indicative of a stalagmite fed by a karst water store of limited volume. Oxygen and carbon isotopes and trace elements generally



have low variability, indicative of a second, well-mixed water source feeding the stalagmite. Stalagmite GM1 provides a high-resolution insight into stalagmite hydrogeochemical responses to environmental change prior to growth hiatuses. Multi-decadal variability of frequency 17–18 years, though statistically not significant at 95% confidence, is present, but only in the growth rate time series, and is slightly less than the range in the growth rate record. A climatic or karstic forcing of this spectral frequency cannot be determined.

Our conceptual model for the stable isotope, trace element and growth rate records in GM1 allows the interpretation of the stalagmite geochemical time series. Importantly, all three proxies were necessary to adequately understand the processes forcing them, and whether they contained a climatic or karstic signal. Only through this approach were we able to confirm that low  $\delta^{18}\text{O}$  at ~129 ka and ~108 ka can be attributed to wetter climatic conditions. These two growth phases occur at the same time as solar insolation maxima for 15°N, and suggest a direct solar forcing on rainfall in Ethiopia at these times, influencing the northward migration of the ITCZ and the associated rain belt of the Indian Summer Monsoon, of potential relevance for early modern human migration out of the region.

## Acknowledgements

Stable isotope analyses were funded by NERC Isotope Geosciences Facility (IP-1099-0509) to AB, AA, CNJ and MJL. Fieldwork to the Mechara caves and subsequent sample preparation (lamina counting, drilling) was supported by START-PACOM grant to AA, a Royal Society grant to AA and AB, and a Leverhulme Trust International Network led by AB. U-Th analyses were supported by a UNSW Early Career Researcher grant to CNJ. The School of Earth Sciences of the Addis Ababa University supported and facilitated fieldwork. AA is grateful to the *Wissenschaftskolleg zu Berlin* where he has been a fellow during the 2017/2018 Academic Year. We thank Henry Lamb and the late Mohammed Umer, who have been very helpful during the successive field trips to the Mechara caves. We would like to particularly recognize the significant contributions of Henry Lamb and Mohammed Umer to understanding the Holocene and Late Pleistocene climate history of Ethiopia. We are grateful to two anonymous reviewers and the editor for the valuable comments that helped to improve the manuscript. Chinese composite and Soreq Cave stalagmite data were obtained from that archived at the World Data Center for Paleoclimatology:

<http://www1.ncdc.noaa.gov/pub/data/paleo/speleothem/asia/china/cheng2016composite.txt>.

[ftp://ftp.ncdc.noaa.gov/pub/data/paleo/speleothem/israel/soreq\\_peqiin\\_2003.txt](ftp://ftp.ncdc.noaa.gov/pub/data/paleo/speleothem/israel/soreq_peqiin_2003.txt).

## Appendix A. Supplementary data

Supplementary data related to this article can be found at <https://doi.org/10.1016/j.quascirev.2018.06.016>.

## References

- Asrat, A., 2012. Speleoseismicity in the Mechara karst, southeastern Ethiopia. In: Fairchild, I.J., Baker, A. (Eds.), *Speleothem Science: from Process to Past Environments*. Wiley-Blackwell (2012).
- Asrat, A., Baker, A., Umer, M., Leng, M.J., van Calsteren, P., Smith, C.L., 2007. A high-resolution multi-proxy stalagmite record from Mechara, Southeastern Ethiopia: paleohydrological implications for speleothem paleoclimate reconstruction. *J. Quat. Sci.* 22, 53–63.
- Asrat, A., Baker, A., Leng, M.J., Gunn, J., Umer, M., 2008. Environmental monitoring in the Mechara Caves, Southeastern Ethiopia: implications for speleothem paleoclimate studies. *Int. J. Speleol.* 37, 207–220.
- Baker, A., Asrat, A., Fairchild, I.J., Leng, M.J., Wynn, P.M., Bryant, C., Genty, D., Umer, M., 2007. Analysis of the climate signal contained within  $\delta^{18}\text{O}$  and growth rate parameters in two Ethiopian stalagmites. *Geochim. Cosmochim. Acta* 71, 2975–2988.
- Baker, A., Asrat, A., Fairchild, I.J., Leng, M.J., Thomas, L.E., Widmann, W., Jex, C., Dong, B., Calsteren, P.V., Bryant, C., 2010. Decadal scale rainfall variability in Ethiopia recorded in an annually laminated, Holocene-age, stalagmite. *Holocene* 20, 827–836.
- Baker, A., Bradley, C., Phipps, S.J., 2013. Hydrological modelling of stalagmite  $\delta^{18}\text{O}$  response to glacial-interglacial transitions. *Geophys. Res. Lett.* 40, 3207–3212.
- Baker, A., Hellstrom, J., Kelly, B.F.J., Mariethoz, G., Trouet, V., 2015. A composite annual-resolution stalagmite record of North Atlantic climate over the last three millennia. *Sci. Rep.* 5 (10307). <http://doi.org/10.1038/srep10307>.
- Baker, A., Flemmons, I., Andersen, M.S., Coleborn, K., Treble, P.C., 2016. What determines the calcium concentration of speleothem-forming drip waters? *Global Planet. Change* 143, 152–161.
- Bar-Matthews, M., Ayalon, A., Kaufman, A., Wasserburg, G.J., 1999. The Eastern Mediterranean paleoclimate as a reflection of regional events: soreq cave, Israel. *Earth Planet Sci. Lett.* 166, 85–95.
- Bar-Matthews, M., Ayalon, A., Gilmour, M., Matthews, A., Hawkesworth, C.J., 2003. Sea-land oxygen isotopic relationships from planktonic foraminifera and speleothems in the Eastern Mediterranean region and their implication for paleorainfall during interglacial intervals. *Geochim. Cosmochim. Acta* 67, 3181–3319.
- Borsato, A., Frisia, S., Fairchild, I.J., Somogyi, A., Susini, J., 2007. Trace element distribution in annual stalagmite laminae mapped by micrometer-resolution X-ray fluorescence: implications for incorporation of environmentally significant species. *Geochim. Cosmochim. Acta* 71, 1494–1512.
- Cheng, H., Edwards, R.L., Chuan-Chou Shen, C.-C., Polyak, V.J., Asmerom, Y., Woodhead, J., Hellstrom, J., Wang, Y., Kong, X., Spötl, C., Wang, X., Alexander Jr., E.C., 2013. Improvements in  $^{230}\text{Th}$  dating,  $^{230}\text{Th}$  and  $^{234}\text{U}$  half-life values, and U–Th isotopic measurements by multi-collector inductively coupled plasma mass spectrometry. *Earth Planet Sci. Lett.* 371–372, 82–91.
- Cheng, H., Edwards, R.L., Broecker, W.S., Denton, G.H., Kong, X., Wang, Y., Zhang, R., Wang, X., 2009. Ice age terminations. *Science* 326, 248–252.
- Cheng, H., Edwards, R.L., Sinha, A., Spötl, C., Yi, L., Chen, S., Zhang, H., 2016. The Asian monsoon over the past 640,000 years and ice age terminations. *Nature* 534, 640–646.
- Degefu, M.A., Rowell, D.P., Bewket, W., 2017. Teleconnections between Ethiopian rainfall variability and global SSTs: observations and methods for model evaluation. *Meteorol. Atmos. Phys.* 129, 173–186.
- Dominguez-Villar, D., Baker, A., Fairchild, I.J., Edwards, R.L., 2012. A method to anchor floating chronologies in annually laminated speleothems with U-Th dates. *Quat. Geochronol.* 14, 57–66.
- Dorale, J.A., Liu, Z., 2009. Limitations of hendy test criteria in judging the paleoclimatic suitability of speleothems and the need for replication. *J. Cave Karst Stud.* 71, 73–80.
- Fleitmann, D., Burns, S.J., Mangini, A., Mudelsee, M., Kramers, J., Villa, I., Neff, U., Al-Subbary, A.A., Buettner, A., Hippler, D., Matter, A., 2007. Holocene ITCZ and Indian monsoon dynamics recorded in stalagmites from Oman and Yemen (Socotra). *Quat. Sci. Rev.* 26, 170–188.
- Genty, D., Quinif, Y., 1996. Annually laminated sequences in the internal structure of some Belgian stalagmite-importance for palaeoclimatology. *J. Sediment. Res.* 66, 275–288.
- Genty, D., Baker, A., Barnes, W.L., 1997. Comparison of annual luminescent and visible laminae in stalagmites. *Comptes Rendus Academie Sciences Paris. Serie II* 325, 193–200.
- Grün, R., Stringer, C., McDermott, F., Nathan, R., Porat, N., Robertson, S., Taylor, L., Mortimer, G., Eggins, S., McCulloch, M., 2005. U-series and ESR analyses of bones and teeth relating to the human burials from Skhul. *J. Hum. Evol.* 49, 316–334.
- Gunn, J., Baker, A., Asrat, A., 2009. Caves of Mechara: the millennium expedition to Ethiopia. *National Speleological Society Journal* 4–7. June 2009.
- Hellstrom, J., 2003. Rapid and accurate U/Th dating using parallel ion-counting multi-collector ICP-MS. *J. Anal. At. Spectrom.* 18, 1346–1351.
- Hellstrom, J., 2006. U–Th dating of speleothems with high initial  $^{230}\text{Th}$  using stratigraphical constraint. *Quat. Geochronol.* 1, 289–295.
- Hershkovitz, I., Weber, G.W., Quam, R., Duval, M., Grün, R., Kinsley, L., Ayalon, A., Bar-Matthews, M., Valladas, H., Norbert Mercier, N., Arsuaga, J.L., Martínón-Torres, M., de Castro, J.M.B., Fornai, C., Martín-Francés, L., Sarig, R., May, H., Krenn, V.A., Slon, V., Rodríguez, L., García, R., Lorenzo, C., Carretero, J.M., Frumkin, A., Shahack-Gross, R., Mayer, D.E.B.-Y., Cui, Y., Wu, X., Peled, N., Groman-Yaroslavski, I., Weissbrod, L., Yeshurun, R., Tsatskin, A., Zaidner, Y., Weinstein-Evron, M., 2018. The earliest modern humans outside Africa. *Science* 359, 456–459.
- Johnson, K.R., Hu, C.Y., Belshaw, N.S., Henderson, G.M., 2006. Seasonal trace-element and stable-isotope variations in a Chinese speleothem: the potential for high-resolution paleomonsoon reconstruction. *Earth Planet Sci. Lett.* 244, 394–407.
- Lamb, H.F., Bates, C.R., Bryant, C.L., Davies, S.J., Huws, D.J., Marshall, M.H., Roberts, H.M., 2018. 150,000-year palaeoclimate record from northern Ethiopia supports early, multiple dispersals of modern humans from Africa. *Sci. Rep.* 8, 1077. <https://doi.org/10.1038/s41598-018-19601-w>.
- Laskar, J., Robutel, P., Joutel, F., Gastineau, M., Correia, A.C.M., Levrard, B., 2004. A long term numerical solution for the insolation quantities of the Earth. *Astron. Astrophys.* 428, 261–285.

- Mariethoz, G., Kelly, B., Baker, A., 2012. Quantifying the value of laminated stalagmites for paleoclimate reconstructions. *Geophys. Res. Lett.* 39, L05407.
- McDougall, I., Brown, F.H., Fleagle, J.G., 2005. Stratigraphic placement and age of modern humans from Kibish, Ethiopia. *Nature* 433, 733–736.
- Nicholson, S.E., 1996. A review of climate dynamics and climate variability in Eastern Africa. In: Johnson, T.C., Odada, E.O. (Eds.), *The Limnology, Climatology and Paleoclimatology of the East African Lakes*, the International Decade for the East African Lakes (IDEAL). Gordon and Breach, Newark, NJ, pp. 25–56.
- Nielsen, R., Akey, J.M., Jakobsson, M., Pritchard, J.K., Tishkoff, S., Willerslev, E., 2017. Tracing the peopling of the world through genomics. *Nature* 541, 302–310.
- Railsback, L.B., Akers, P.D., Wang, L., Holdridge, G.A., Voarintsoa, N.R., 2013. Layer-bounding surfaces in stalagmites as keys to better paleoclimatological histories and chronologies. *Int. J. Speleol.* 42, 167–180.
- Taye, M.T., Willems, P., 2012. Temporal variability of hydroclimatic extremes in the Blue Nile basin. *Water Resour. Res.* 48, W03513.
- Tierney, J.E., de Menocal, P.B., Zander, P.D., 2017. A climatic context for the out-of-Africa migration. *Geology*. <https://doi.org/10.1130/G39457.1>.
- Timmermann, A., Friedrich, T., 2016. Late Pleistocene climate drivers of early human migration. *Nature* 538, 92–95.
- Treble, P.C., Schmitt, A.K., Edwards, R.L., McKeegan, K.D., Harrison, T.M., Grove, M., Cheng, H., Wang, Y.J., 2007. High resolution secondary ionisation mass spectrometry (SIMS)  $\delta^{18}\text{O}$  analyses of Hulu cave speleothem at the time of heinrich event 1. *Chem. Geol.* 238, 197–212.
- Tribolo, C., Asrat, A., Bahain, J.-J., Chapon, C., Douville, E., Fragnol, C., Hernandez, M., Hovers, E., Leplongeon, A., Martin, L., Pleurdeau, D., Pearson, O., Puaud, S., Assefa, Z., 2017. Across the gap: geochronological and sedimentological analyses from the Late Pleistocene-Holocene sequence of Goda Buticha, Southeastern Ethiopia. *PLoS One* 12, e0169418.
- Voarintsoa, N.R.G., Railsback, L.B., Brook, G.A., Wang, L., Kathayat, G., Cheng, H., Li, X., Edwards, R.S., Rakotondrazafy, A.F.M., Razanatseho, M.O.M., 2017. Three distinct Holocene intervals of stalagmite deposition and nondeposition revealed in NW Madagascar, and their paleoclimate implications. *Clim. Past* 13, 1771–1790.
- White, T.D., Asfaw, B., Degusta, D., Gilbert, H., Richards, G.D., Suwa, G., Howell, F.C., 2003. Pleistocene *Homo sapiens* from middle Awash, Ethiopia. *Nature* 423, 742–747.